

Three-dimensional ferroelectric domain imaging of epitaxial BiFeO₃ thin films using angle-resolved piezoresponse force microscopy

Moonkyu Park,^{1,3} Seungbum Hong,^{1,a)} Jeffrey A. Klug,^{1,4} Michael J. Bedzyk,^{1,4,5} Orlando Auciello,^{1,2} Kwangsoo No,^{3,a)} and Amanda Petford-Long²

¹Materials Science Division, Argonne National Laboratory, Argonne, Illinois 60439, USA

²Center for Nanoscale Materials, Argonne National Laboratory, Argonne, Illinois 60439, USA

³Department of Materials Science and Engineering, Korea Advanced Institute of Science and Technology, Daejeon 305-701, Republic of Korea

⁴Department of Physics and Astronomy, Northwestern University, Illinois 60208, USA

⁵Department of Materials Science, Northwestern University, Illinois 60208, USA

(Received 12 May 2010; accepted 16 August 2010; published online 17 September 2010)

Here we introduce angle-resolved piezoresponse force microscopy (AR-PFM), whereby the sample is rotated by 30° increments around the surface normal vector and the in-plane PFM phase signals are collected at each angle. We obtained the AR-PFM images of BaTiO₃ single crystal and cube-on-cube epitaxial (001) BiFeO₃ (BFO) thin film on SrRuO₃/SrTiO₃ substrate, and confirmed that the AR-PFM provides more unambiguous information on the in-plane polarization directions than the conventional PFM method. Moreover, we found eight additional in-plane polarization variants in epitaxial BFO thin films, which are formed to mitigate highly unstable charged domain boundaries. © 2010 American Institute of Physics. [doi:10.1063/1.3487933]

Ferroelectric oxide materials provide a unique platform to enable the next generation memory devices, using their switchable polarization and integration of ferroelectric nanocapacitors.¹ Until now, the SrBi₂Ta₂O₉ (SBT) (Refs. 2 and 3) and Pb(Zr_xTi_{1-x})O₃ (PZT) (Ref. 3) family of materials have served as the cornerstone for applications in non-volatile memories and piezoelectric actuators (PZT). A critical drawback of SBT is the relatively low polarization (~30 μC/cm²) (Refs. 2 and 3) while the problem with PZT is the presence of lead. In this respect, the lead-free ferroelectric BiFeO₃ (BFO) has attracted a great deal of attention because of its superior polarization (~120 μC/cm²),^{4,5} which is comparable to that of the tetragonal, Ti-rich PZT films.

However, BFO thin films exhibit high leakage currents,⁶ where oxygen vacancies⁷ and/or the unusual electronic transport through ferroelectric domain walls are the main cause.⁸ Hong *et al.*⁹ also observed the emergence of charged domain boundaries (CDBs) in round-shaped BFO nanostructures, which contributed to leaky piezoresponse hysteresis loops. While the leakage paths formed at the CDBs ($\sum \mathbf{P} \cdot \mathbf{n} \neq 0$) in BFO have been reported, it is still not clear why the CDBs form and how they affect the piezoresponse at the nanoscale. Therefore, an in-depth investigation of the domain structure by piezoresponse force microscopy (PFM) in BFO thin films is required, which helps us understand the mechanism of polarization switching and electrical properties. However, constructing three-dimensional PFM images of polarization domains has been a great challenge because sliding of the tip and cantilever buckling influence the PFM signals.^{10,11}

Here we introduce a polarization domain imaging technique named angle-resolved piezoresponse force microscopy (AR-PFM), present direct observation of CDBs and intermediate polarization variants in epitaxially grown BFO thin

films, and discuss the correlation between the resulting domain configuration and the film growth mechanism.

Figure 1(a) shows the schematic by which we constructed the in-plane (IP) ferroelectric domain images using AR-PFM. First, we aligned a specific crystallographic orientation ([100]) of either the BTO single crystal or the BFO film with the cantilever scan direction and then obtained the IP and out-of-plane (OP) PFM phase and amplitude signals after each rotation around the film surface normal, from 0° to 180° with an interval of 30° between each domain image. We identified each IP polarization vector by finding the area where the phase contrast changed by 180° after two adjacent rotations of the sample, and denoted the IP component of the polarization vector for that area as lying between the scan directions before and after the phase reversal. For example, in Fig. 1(a) we see initiation of a phase reversal for a rotation angle of 90° when we have a single domain with IP polarization, which is perpendicular to the reference scan axis

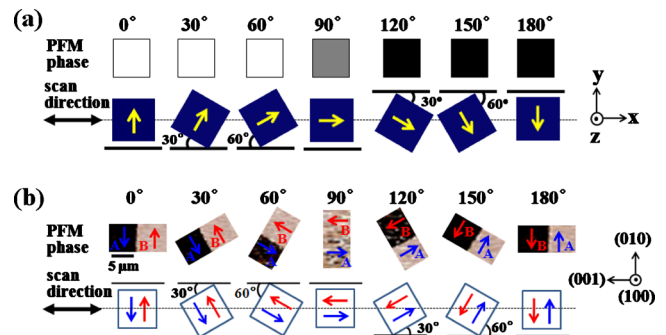


FIG. 1. (Color online) (a) Schematics showing the working principle of the AR-PFM method. The yellow arrows inside the blue square boxes show the IP polarization directions of the sample at θ between 0° and 180°. The x-axis is the scan direction and the z-axis is the film surface normal. The dashed line is a guide for the eye to compare the scan and the IP polarization directions. (b) IP PFM phase images of (100) BaTiO₃ single crystal at various θ between 0° and 180° and their schematic representations of IP polarization directions. The dark gray (blue) and light gray (red) arrows represent the IP polarization direction of domains A and B.

^{a)}Authors to whom correspondence should be addressed. Electronic addresses: hong@anl.gov and ksno@kaist.ac.kr.

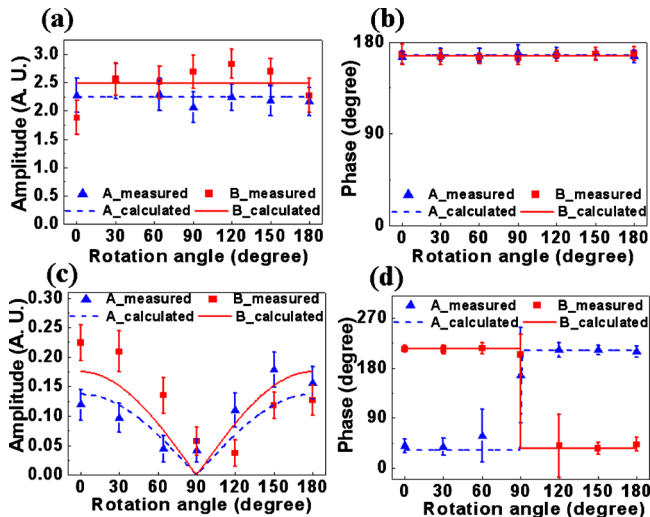


FIG. 2. (Color online) OP PFM (a) amplitude and (b) phase, and IP PFM (c) amplitude and (d) phase values of (100) BaTiO₃ single crystal as a function of θ . Dark gray (blue) triangle and light gray (red) square represent the experimentally measured values of domains A and B in Fig. 1(b), respectively. The dark gray (blue) dashed line and light gray (red) solid line show the calculated values for domains A and B, respectively.

(0°). The AR-PFM technique therefore allows us to determine all the IP polarization directions within the angular resolution of each step (30° in this study) without relying on PFM amplitude information.

We used the AR-PFM technique to study the polarization domains of a (100) BaTiO₃ single crystal (MTI Corporation) as a standard example to check whether we can reliably identify the IP polarization directions.¹² We chose a region comprised of (0 $\bar{1}$ 0) (region A) and (010) (region B) polarization variants and rotated the region by 30° between recording each set of images [Fig. 1(b)]. Here we defined the angle of sample rotation, θ , as that between the cantilever long axis and the [001] direction. We found that the phase reversal occurred near $\theta=90^\circ$ in both regions A and B, which verifies that AR-PFM can unambiguously determine the IP polarizations within the resolution of each angular step.

We plotted the average IP and OP PFM phase and amplitude values over the whole area in regions A and B in Fig. 1(b), as a function of θ [Figs. 2(a)–2(d)]. As expected, the OP PFM amplitude and phase values in both regions remained constant regardless of θ because the OP piezoresponse component does not change with IP rotation of the sample [Figs. 2(a) and 2(b)]. However, the IP PFM amplitude deviated from its expected dependence on θ [see Fig. 2(c)]. This discrepancy will lead to inaccurate domain images if we use the amplitude and phase of IP PFM images to reconstruct the polarization directions in the domains. The PFM phase information, however, is relatively stable and behaves more consistently with the theory [Fig. 2(d)]. Therefore, AR-PFM, which is based on the PFM phase contrast and θ , is expected to yield a more accurate picture of IP domain polarization vectors.

We fabricated BFO multiferroic thin films to identify the ferroelectric polarization variants using the AR-PFM method. BFO thin films (40 nm thick) were grown by rf magnetron sputtering (AJA International, Rapier Series) at 680 °C over a 120 nm thick SrRuO₃ (SRO) (001) bottom electrodes deposited on SrTiO₃ (STO) (001) substrates at 680 °C. X-ray diffraction (XRD) Phi scans of the BFO,

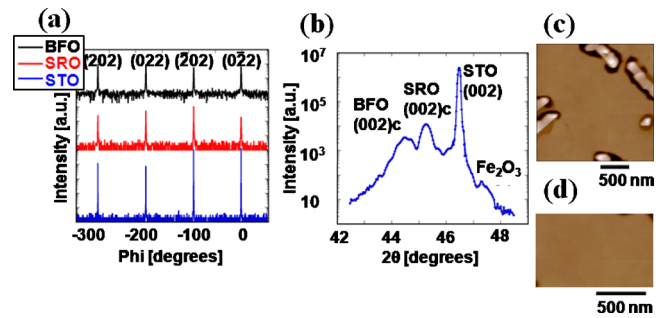


FIG. 3. (Color online) (a) IP and (b) OP XRD plots of (001) BiFeO₃ thin film grown on (001) SRO/(001) STO substrate. AFM topography images of (c) (001) BiFeO₃ thin film and (d) the selected area for AR-PFM domain image acquisitions.

SRO, and STO (202) family of reflections confirmed cube-on-cube epitaxy for both the BFO and SRO films [Fig. 3(a)]. The θ -2 θ scan also showed that the BFO and SRO films are both pseudocubic (001) oriented [Fig. 3(b)]. The XRD analysis showed that there was no IP rotation of the crystals, suggesting there would be no associated IP polarization rotation.

There was a small amount of Fe₂O₃ impurity present in the films, as seen from the θ -2 θ XRD scan, which is consistent with the faceted islands that are seen in the atomic force microscopy (AFM) topography image [Fig. 3(c)], and is in agreement with recent findings that the BFO and Fe₂O₃ phases coexist when BFO thin films are grown at oxygen pressures below or equal to 5 mTorr.¹³ In order to avoid any spurious effects caused by the Fe₂O₃ phase and surface morphology, we chose to analyze a flat area of $1.17 \times 0.74 \mu\text{m}^2$, which is free of Fe₂O₃, when acquiring the AR-PFM domain images [Fig. 3(d)].

We verified the IP polarization variants of the BFO thin film using AR-PFM (Fig. 4). The region in which the phase changed by 180° after a rotation step of 30° was painted with a different color on each IP PFM phase image. Since the OP PFM signals showed a uniform downward polarization orientation for all the angular steps,¹² we could map all the polarization by superimposing the regions where the phase signals changed by 180° at each angular step [Fig. 4(a)]. As a result, we identified twelve polarization variants in BFO thin films whereas a number of studies have reported that

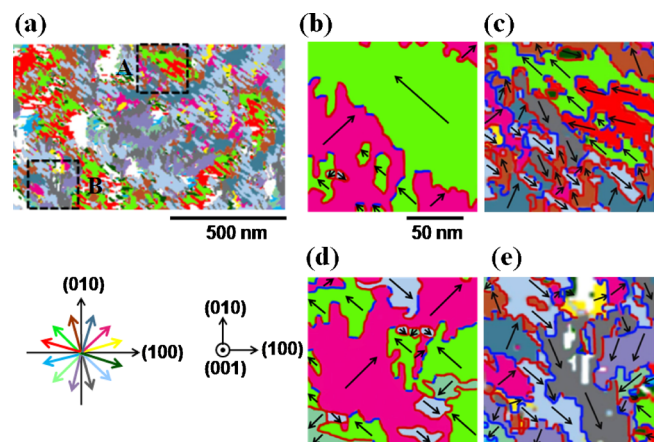


FIG. 4. (Color online) (a) IP domain configuration of BiFeO₃ thin film. Local ferroelectric domain configurations constructed by [(b) and (d)] conventional PFM and [(c) and (e)] AR-PFM in the regions A [(b) and (c)] and B [(d) and (e)] in Fig. 4(a). Dark gray (blue) and light gray (red) lines represent neutral and CDBs, respectively.

BFO can only have up to eight polarization variants lying along the $\langle 111 \rangle$ directions.^{14,15} This result shows that the epitaxial BFO thin films used in this study have regions with polarization variants deviating from the $\langle 111 \rangle$ directions, which are the easy polarization axes analogous to easy magnetization axes.¹⁵ Without using the AR-PFM technique, it would have been difficult to find those intermediate polarization variants due to the large errors in amplitude signals obtained using conventional lateral PFM.¹⁰

In order to understand the origin of intermediate polarization variants and study the local distribution of ferroelectric domains, we constructed the domain map of the regions (A) and (B) in Fig. 4(a) using the conventional PFM [Figs. 4(b) and 4(d)] and the AR-PFM methods [Figs. 4(c) and 4(e)]. Imaging of the domain configuration by the conventional PFM method, based on the assumption of four IP polarization variants, showed a large portion of CDBs that would be very unstable due to the increase in the electrostatic energy at the boundaries. The proportion of CDBs was 86.3% in region A and 80.2% in region B, respectively, in Figs. 4(b) and 4(d). However, when constructing the domain configuration from our AR-PFM data, the proportion of CDBs decreased to 63.3% in region A and 43.6% in region B [Figs. 4(c) and 4(e)]. In addition to the decrease in the portion of CDBs, the amount of charging along the CDBs would also decrease due to the smaller angle between the neighboring polarization variants separated by the CDBs.

It is relevant to discuss the possible origin of the CDBs and their impact on the ferroelectric properties of BFO films. Since BFO has a Curie temperature (1100 K) above the growth temperature (953 K), BFO nuclei formed during the initial stages in film growth, larger than the critical size (e.g., 4.2 nm for PbTiO_3 particles) (Ref. 16) to exhibit polarization, will have their own ferroelectric polarization variants when they are deposited on the SRO/STO substrate. At this stage, stable polarization vectors pointing along $\langle 111 \rangle$ directions are induced by the rhombohedral crystal symmetry of the nuclei. As the film grows first in an island mode, each island with its polarization variant will not interact with the neighboring ones and grow independently, preserving their polarization variants, until they touch each other. It is highly likely that in this process many of the polarization directions in the grains will not be able to fully switch to form a neutral boundary with the adjacent regions and so CDBs will form. We believe that the intermediate polarization variants, which deviate from the easy axes imposed by the rhombohedral crystal symmetry, are formed to act as mitigating regions to decrease the electrostatic energy at the CDBs, as in the case of vortex domain configuration.¹⁷ The CDBs that remain even after the formation of the intermediate variants are expected to be the dominant sources of imprint and high leakage properties in the films.

It could be argued that when the ferroelectric islands were initially deposited on the substrate they would have no preferred IP polarization direction because of the pseudocubic symmetry, which is not the case if the film was grown in a layer by layer deposition mode where the initial preferential polarization variants would dominate the domain pattern. In order to check the validity of our results, we analyzed the areal fraction of each IP polarization direction [Fig. 4(a)]. We found that the relative fractions of domains with positive $([010])$ and negative $([0\bar{1}0])$ y-axis IP polarization vector

components were 42% and 58%, respectively, whereas those of domains with positive $([100])$ and negative $([\bar{1}00])$ x-axis IP polarization vector components were 57% and 43%, respectively. These findings support the hypothesis that the ferroelectric domains did not have a significant preference to a specific polarization direction at initial growth stage.

In conclusion, we found 12 IP polarization variants in an epitaxially grown, (001) BFO thin film on SRO/STO substrates, using the AR-PFM method. The emergence of the additional variants deviating from the so-called ferroelectric easy axes, which are formed to mitigate highly unstable CDBs, lead to formation of continuous domain structure resembling Neel type domain walls, where the polarization variants rotate around the vector normal to them.

The submitted manuscript has been created by UChicago Argonne, LLC, Operator of Argonne National Laboratory (“Argonne”). Argonne, a U.S. Department of Energy Office of Science laboratory, is operated under Contract No. DE-AC02-06CH11357. The U. S. Government retains for itself, and others acting on its behalf, a paid-up nonexclusive, irrevocable worldwide license in said article to reproduce, prepare derivative works, distribute copies to the public, and perform publicly and display publicly, by or on behalf of the Government. The XRD facility at NU is supported by MR-SEC Grant No. DMR-0520513 from the National Science Foundation. M.P. and K.N. acknowledge the financial support by Mid-career Researcher Program (Grant No. 2010-0015063) and Nano R&D Program (Grant No. 2009-0081946) through NRF grant funded by the MEST. We thank Professor A. Gruverman at University of Nebraska for his critical reading of our manuscript.

¹C. H. Ahn, K. M. Rabe, and J. M. Triscone, *Science* **303**, 488 (2004).

²J. F. Scott and C. Paz de Araujo, *Science* **246**, 1400 (1989).

³O. Auciello, J. F. Scott, and R. Ramesh, *Phys. Today* **51**(7), 22 (1998).

⁴J. Wu and J. Wang, *J. Appl. Phys.* **106**, 104111 (2009).

⁵J. Wang, J. B. Neaton, H. Zheng, V. Nagarajan, S. B. Ogale, B. Liu, D. Viehland, V. Vaithyanathan, D. G. Schlom, U. V. Waghmare, N. A. Spaldin, K. M. Rabe, M. Wuttig, and R. Ramesh, *Science* **299**, 1719 (2003).

⁶J. Dho, X. Qi, H. Kim, J. L. MacManus-Driscoll, and M. G. Blamire, *Adv. Mater.* **18**, 1445 (2006).

⁷S. K. Singh, K. Maruyama, and H. Ishiwaru, *Appl. Phys. Lett.* **91**, 112913 (2007).

⁸J. Seidel, L. W. Martin, Q. He, Q. Zhan, Y.-H. Chu, A. Rother, M. E. Hawkrige, P. Maksymovych, P. Yu, M. Gajek, N. Balke, S. V. Kalinin, S. Gemming, F. Wang, G. Catalan, J. F. Scott, N. A. Spaldin, J. Orenstein, and R. Ramesh, *Nature Mater.* **8**, 229 (2009).

⁹S. Hong, J. A. Klug, M. Park, A. Imre, M. J. Bedzyk, K. No, A. Petford-Long, and O. Auciello, *J. Appl. Phys.* **105**, 061619 (2009).

¹⁰S. V. Kalinin, B. J. Rodriguez, S. Jesse, J. Shin, A. P. Baddorf, P. Gupta, H. Jain, D. B. Williams, and A. Gruverman, *Microsc. Microanal.* **12**, 206 (2006).

¹¹R. Nath, S. Hong, J. A. Klug, A. Imre, M. J. Bedzyk, R. S. Katiyar, and O. Auciello, *Appl. Phys. Lett.* **96**, 163101 (2010).

¹²See supplementary material at <http://dx.doi.org/10.1063/1.3487933> for detailed experimental conditions of PFM measurements.

¹³M. Murakami, S. Fujino, S.-H. Lim, L. G. Salamanca-Riba, M. Wuttig, I. Takeuchia, B. Varughese, H. Sugaya, T. Hasegawa, and S. E. Lofland, *Appl. Phys. Lett.* **88**, 112505 (2006).

¹⁴F. Zavaliche, P. Shafer, R. Ramesh, M. P. Cruz, R. R. Das, D. M. Kim, and C. B. Eom, *Appl. Phys. Lett.* **87**, 252902 (2005).

¹⁵Y. Chu, L. W. Martin, M. B. Holcomb, and R. Ramesh, *Mater. Today* **10**, 16 (2007).

¹⁶W. L. Zhong, Y. G. Wang, P. L. Zhang, and B. D. Qu, *Phys. Rev. B* **50**, 698 (1994).

¹⁷A. Gruverman, D. Wu, H.-J. Fan, I. Vrejoiu, M. Alexe, R. J. Harrison, and J. F. Scott, *J. Phys.: Condens. Matter* **20**, 342201 (2008).